Orbit Determination of the Near-Earth Asteroid 2012 FN62 Using the Method of Gauss

Adam Banks, Noah Lee, Vincent Zheng

The Summer Science Program – Team Sigma Noodles

Abstract

Near-Earth asteroids are often perturbed from their orbits and thus pose the potentially catastrophic threat of collisions with Earth. Therefore, it is crucial to precisely track their orbits over time. Over several weeks, we observed the near-Earth asteroid 2012 FN62 six times. Then, we applied image reduction, centroiding, aperture photometry, and least squares plate reduction (LSPR) to the best image taken during each of the three clearest observations to calculate the right ascension and declination of 2012 FN62 at the time the image was taken. Afterward, we wrote a Python script to compute the orbital elements of the asteroid using the Method of Gauss and ran 1,000,000 Monte Carlo simulations to determine the uncertainty of the computed values. The computed orbital elements of 2012 FN62 are:

- Semi-Major Axis Length: 3.3 AU ± 0.1 AU
- Eccentricity: 0.615 ± 0.011
- Longitude of Ascending Node: 147.95° ± 0.02°
- Inclination: 10.00° ± 0.11°
- Argument of Perihelion: 142.47° ± 0.06°
- Mean Anomaly (at 06:05:09 UT on 6/25/2024): 356.60° ± 0.14°
- Time of Last Perihelion Passage: 2458361.2 Julian days ± 0.1 Julian days

Finally, we ran 2,000 numerical orbital integration simulations using REBOUND to determine the possible fates of 2012 FN62. We found that over the next 50 million years, 2012 FN62 has a:

- 91.60% chance of being ejected from the Solar System
- 6.60% chance of colliding with the Sun
- 1.10% chance of colliding with Jupiter
- 0.50% chance of surviving all 50 million years
- 0.15% chance of colliding with Saturn
- 0.05% chance of colliding with Venus

1. Introduction

The Solar System is crowded with astronomical debris such as dust, comets, asteroids, and recently, man-made satellites. Comets, primarily found within the trans-Neptunian Kuiper Belt and the remote Oort Cloud, are composed of ice, dust, rock, and frozen gases. These comets follow highly eccentric orbits that rarely bring them close to the inner Solar System. As such, the approach of any comet – for instance the famous Halley's Comet – near Earth is a noteworthy celestial event. On the other hand, asteroids are generally found much closer to the Sun than comets, with most being located between Mars and Jupiter in a region known as the Asteroid Belt. As such, asteroids are much more likely to venture into the inner Solar System and approach the Earth. Asteroids that come within 1.3 astronomical units (AU) – 194 million kilometers – of the Sun are considered Near-Earth Asteroids (NEAs) and are of significant interest.

The Earth has seen countless asteroid impacts over its history – the most famous being the one responsible for the extinction of the dinosaurs approximately 66 million years ago. More recently, there have been major impacts over cities such as Tunguska and Chelyabinsk. Even though both of these NEAs were relatively small, they caused widespread damage and devastation. Thus, impacts from large asteroids would be catastrophic to human civilization.

Although the orbits of almost all large NEAs have been determined, most of the smaller "city killers" follow unknown trajectories. Additionally, as asteroids are often perturbed, their orbits should frequently be updated. Search campaigns run by organizations such as the International Astronomical Search Collaboration combine the efforts of amateur and professional astronomers as they scan the skies for any asteroid that could threaten Earth [1]. To contribute to such research, we observed the near-Earth asteroid 2012 FN62 over the course of five weeks and determined its orbit using the Method of Gauss.

In this paper, section 2 defines the orbital elements and the Method of Gauss, section 3 examines the processes of observation, image reduction, centroiding, aperture photometry, and LSPR that were performed on the images, section 4 contains the results of the process, and section 5 discusses them.

2. The Method of Gauss

2.1. The Orbital Elements

Every orbit around the Sun is determined by six constants known as orbital elements.

As stated in Kepler's first law, objects orbit the Sun in a elliptical orbits with the Sun at one focus. The first two orbital elements – the length of the semi-major axis (a) and the eccentricity (e) – determine the size and shape of the ellipse.

The orientation of the orbital plane is defined by the third and fourth orbital elements, the inclination (i) and the longitude of the ascending node (Ω). The inclination is the angle from the ecliptic to the orbital plane, with an inclination above 90° corresponding to a retrograde orbit. The longitude of the ascending node is the angle from the vernal equinox to the ascending node – the point at which the object transitions from being below to above the ecliptic.

The fifth orbital element, the argument of perihelion (ω), is the angle from the ascending node to the perihelion, the point in the orbit closest to the Sun. This element fixes the orientation of the orbit within the plane.

The final orbital element is the mean anomaly (M), which determines the location of the object in its orbit. Consider a fictional object traveling along the auxiliary circle of the orbit of the real object with the same period. The mean anomaly is the angle from the perihelion to the location of this fictional object. *Because both objects have the same period, the location of the real object can be computed based on the mean anomaly.*

Though not an orbital element, the time of last perihelion passage (T), the Julian date of the object's most recent crossing of its perihelion, is also often reported alongside them. [2]

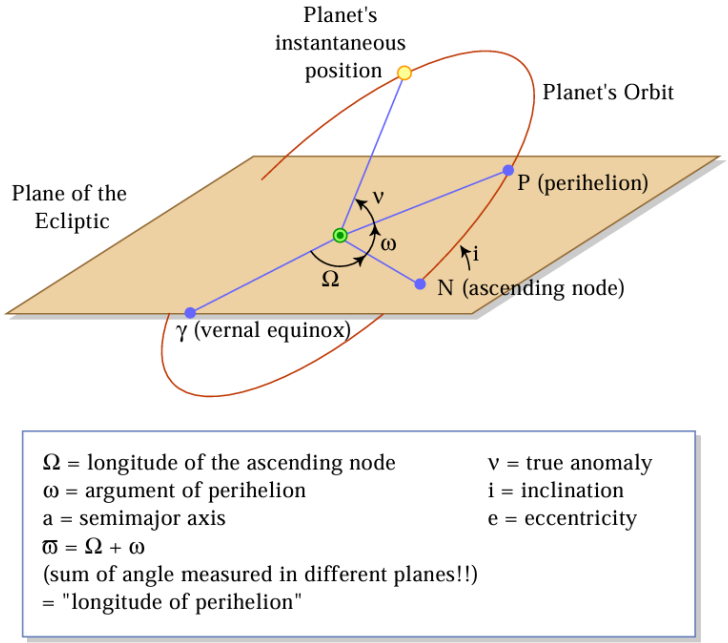


Figure 1: The Orbital Elements [3]

2.2. The Method of Gauss

The Method of Gauss (MoG) applies vector and algebraic manipulation to three clear observations spaced multiple days apart to determine the orbital elements of a celestial body's orbit around the Sun.

First, it considers the fundamental triangle, which is formed by the Earth to Sun vector $\vec{R}$, the Earth to asteroid vector $\vec{\rho}$, and the Sun to asteroid vector $\vec{r}$:

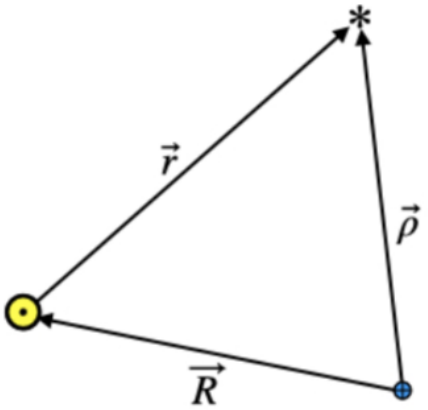


Figure 2: The Fundamental Triangle [2]

Evidently,

$$\vec{r} = \vec{\rho} - \vec{R} = \rho\hat{\rho} - \vec{R} \tag{1}$$

Additionally, $\hat{\rho}$ is given by

$$\hat{\rho} = (\cos\alpha\cos\delta)\hat{i} + (\sin\alpha\cos\delta)\hat{j} + (\sin\delta)\hat{k} \tag{2}$$

and $\vec{R}$ is known. Thus, ρ is the only unknown. Once ρ is determined, $\vec{r}$ and $\dot{\vec{r}}$ can be computed, which allows the orbital elements to be calculated using the formulas in appendix B. The Method of Gauss computes $\vec{r}$ and $\dot{\vec{r}}$ from three observations.

For each of the observations, the Gaussian time τ alongside the right ascension α and the declination δ of the body are recorded (the process for finding α and δ is discussed later in this text), and $\hat{\rho_1}$, $\hat{\rho_2}$, and $\hat{\rho_3}$ are computed using equation 2.

Next, vector manipulation is used to calculate a rough approximation of ρ_2. Then, ρ_2 is used to get an approximation of $\vec{r_2}$ using equation 1. Next, $\vec{r_2}$ is used to improve the approximation of ρ_2, which is used to improve the approximation of $\vec{r_2}$. This process it repeated until $\vec{r_2}$ converges. Finally, $\vec{r_2}$ can be used to calculate $\dot{\vec{r_2}}$ and the orbital elements. [2]

Equations used in the Method of Gauss are given in Appendix A, and those used in the calculation of the orbital elements are given in Appendix B. However, their derivations are not discussed within this text.

3. Observations and Image Processing

3.1. Data Acquisition

2012 FN62 was observed from Morehead Observatory at the University of North Carolina at Chapel Hill, located at $\phi = 35^o\ 54^{'}\ 47.5200^{"}$ N, $\lambda = 79^o\ 3^{'}\ 21.0492^{"}$ W. The telescope has a 0.61 meter aperture primary mirror with a focal ratio of 3.5. The secondary mirror has a 0.18 meter aperture, which provides the entire telescope with a full focal ratio of 13.5. It is mounted on an equatorial mount and utilizes a parabolic Cassegrain reflector structure. [4]

The telescope's camera is a 9.3 megapixel (3056 pixels by 3056 pixels), 36.6 by 36.6 millimeter charge-coupled device (CCD) with a pixel size of 12 micrometers and a pixel scale of 0.3 arcseconds per pixel. Liquid cooled to a temperature of -20°C, it is most efficient around the 580 nanometer wavelength of light, has an 8 MHz digitization speed, captures full 16-bit resolution images, and has flexible binning and readout. The noise rate is 15 electrons per second [5].

After utilizing the software MaxIm DL [6] to take images, they were processed through AstroImageJ (AIJ) [7] using calibration flats, biases, and darks. AIJ and SAOImageDS9 [8] were utilized to search for and locate 2012 FN62 by blinking between the images and searching for a blur that was moving in a different direction than the rotation of the sky, as illustrated in figure 4.

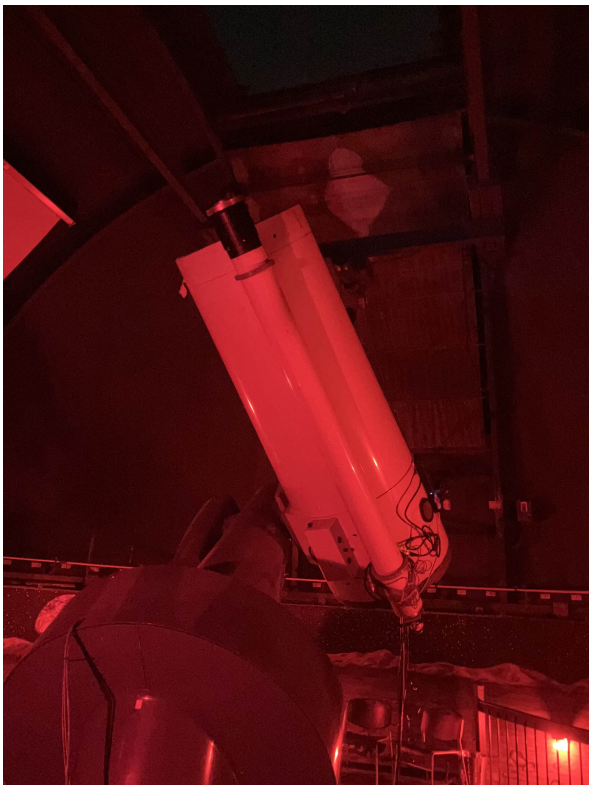


Figure 3: Telescope at Morehead Observatory, University of North Carolina at Chapel Hill [2]

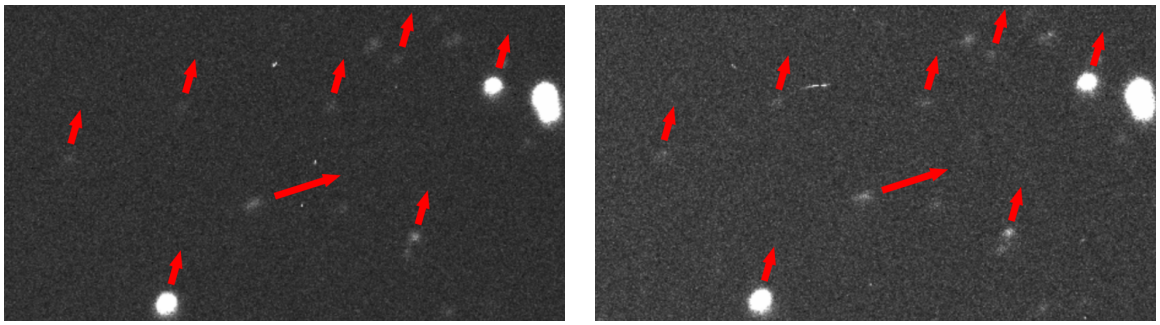


Figure 4: Movement of 2012 FN62 on June 14, 2024

Table 1: Observations of 2012 FN62

Date	Time Window (UT)	Weather	Atmospheric Seeing	Image Usability
6/12	2:30 - 3:30	Good	Average	Poor
6/14	5:30 - 6:30	Superior	Good	Good
6/22	5:30 - 6:30	Good	Average	Poor
6/25 [9]	4:30 - 5:30	Good	Average	Good
6/29	3:30 - 4:30	Good	Average	Average
7/2	5:30 - 6:30	Superior	Good	Superior

Table 2: Best Image from Each Observation – Position Data from JPL Horizons [10]

Date	Time (UT)	Predicted Position (α, δ)	Duration	Image Used in OD
6/12	3:14:22	(17:40:00.10, +13° 09' 30.0")	300s	No
6/14	6:02:20	(17:42:34.38, +13° 18' 40.3")	300s	Yes
6/23	6:10:12	(17:54:50.98, +13° 12' 09.2")	300s	No
6/25	6:05:09	(17:57:54.87, +12° 59' 38.1")	300s	Yes
6/29	4:08:53	(18:04:20.38, +12° 22' 08.7")	180s	No
7/2	6:02:37	(18:09:47.43, +11° 40' 05.6")	300s	Yes

[1]

3.2. Image Reduction

CCDs capture electrons from the sky in gravitational potential wells to measure the brightness of the received signal. Wells are read out individually to a computer to create the image. CCDs are affected by three main sources of error: read noise, dark current, and non-illumination. Additionally, to avoid negative values caused by random noise, a large number, called bias, is added to the value in each cell. Although not a source of error, bias must also be accounted for during the process of image reduction.

[1]The Method of Gauss requires three observations. The reasoning for the selection is discussed in section 4.1.

Read noise is the error caused by the reading of the electrons in the potential wells by the detector. Unfortunately, read noise is not correctable through image calibration.

Dark current is the flow of electrons into the potential wells due to thermal energy in the CCD rather than energy from photons. To account for dark current, exposure images are taken with the shutter closed in order to isolate the dark current.[2] These images are called "darks". Taking many darks and calculating the median value in each pixel results in a master dark,[3] which can be subtracted from the original image to correct for the dark current — in addition, since all images include bias, this subtraction also accounts for the bias in the original image. The effects of dark current can also be reduced by lowering the temperature of the CCD.

Finally, non-illumination occurs when light fails to reach the CCD due to illumination anomalies such as vignette and filter dust. Non-illumination can be corrected by exposure images pointed at an area of uniform brightness, most commonly the twilight sky opposite the setting sun. These images, called "flats", isolate sources of non-illumination. Taking many flats and calculating the median value in each pixel results in a master flat. After subtracting the master bias, the master flat is normalized to determine the proportion of light that reaches each pixel compared to what should be expected. Finally, non-illumination can be accounted for by dividing the dark current corrected image by the normalized master flat.

The calibrated image can now be used in the processes of photometry and astrometry. [11]

3.3. Astrometry - Centroiding

Astrometry is the measurement of the locations of celestial objects [12]. Astrometry was used in the analysis of 2012 FN62 to calculate the (x, y) pixel center of 2012 FN62 on each image through the method of centroiding.

To begin, the asteroid was located on the image and an approximate center was estimated. An aperture with a radius between 0.75 to 1 full width half maximum (FWHM) was drawn around the center, enclosing between 79% to 94% of the light reflected off the asteroid. However, the aperture includes the sky background noise which must be calculated and removed. After padding the aperture by half of a half width half maximum (HWHM), an annulus one HWHM wide is drawn around the padding. The sky background noise was determined by finding the median of the values of all pixels in the annulus. After subtracting the sky background noise from all pixels in the aperture, the centroid was calculated by finding the weighted average of the values contained in the pixels in the aperture, given by

$$\bar{x} = \frac{\sum_{aperture} N_e x_i}{\sum_{aperture} N_i}, \bar{y} = \frac{\sum_{aperture} N_e y_i}{\sum_{aperture} N_e} \tag{3}$$

where N_e is the value contained in a pixel in the aperture, and x_i and y_i are the pixel's coordinates on the image. [12]

Both manual centroiding and automated centroiding through AIJ were performed. In the end, the results from AIJ were used as the final pixel centroids of 2012 FN62 on the images.

[2] Since the dark current is related to temperature, darks must be taken with the CCD at the same temperature as the real images.

[3] The master dark and the normalized master flat used in the reduction of 2012 FN62 are provided in Appendix D.

3.4. Photometry - Aperture Photometry

Photometry is the measurement of the intensity of light. In the analysis of 2012 FN62, photometry was used to calculate the instrumental and apparent magnitudes of the asteroid through the method of aperture photometry.

An aperture and annulus of similar sizes as in centroiding were drawn around the centroid of the asteroid. The sky background noise was also calculated in the same manner. The total signal from the source (S) is given by

$$S = \sum_{aperture} (N_e) - n_{ap} S ky_e \tag{4}$$

where n_{ap} is the total number of pixels in the aperture and $S ky_e$ is the median background noise. [13]

For each analyzed image, seven reference stars in close vicinity to 2012 FN62 were selected for analysis. The value of the signal minus the sky background ($S - S ky_e$) was measured for each reference star and the asteroid using AIJ, then SAOImageDS9 was used to find the R-magnitude m_R of each star (R-magnitude was used because the spectral response of the CCD is similar to an R-filter). Plotting m_R against $\log S$ for each star, a linear regression was performed and the result was used to calculate the R-magnitude of the asteroid.

Table 3: Linear Regressions of m_R Against $\log S$

Date	Reference Stars	Linear Regression	$\log(S_{2012FN62})$	m_R
6/14	7	-2.49x + 27.7	4.204	17.23
6/25	7	-2.67x+28.6	4.314	17.08
7/2	7	-2.93x + 27.9	3.750	16.91

3.5. Astrometry - Least Squares Plate Reduction

When analyzing 2012 FN62, astrometry was also used in the conversion of the (x, y) center of the asteroid on the image to a (α, δ) location on the celestial sphere through the method of least-squares plate reduction (LSPR). LSPR assumes that the transformation $(x, y) \rightarrow (\alpha, \delta)$ is given by the linear transformation

$$\begin{bmatrix} \alpha \\ \delta \end{bmatrix} = \begin{bmatrix} b_1 \\ b_2 \end{bmatrix} + \begin{bmatrix} a_{11} & a_{12} \\ a_{21} & a_{22} \end{bmatrix} \begin{bmatrix} x \\ y \end{bmatrix} \tag{5}$$

Solving for $b_1, b_2, a_{11}, a_{12}, a_{21}, a_{22}$ as in Appendix C,

$$\begin{bmatrix} b_1 \\ a_{11} \\ a_{12} \end{bmatrix} = A^{-1} \begin{bmatrix} \Sigma\alpha_i \\ \Sigma\alpha_i x_i \\ \Sigma\alpha_i y_i \end{bmatrix}, \begin{bmatrix} b_2 \\ a_{21} \\ a_{22} \end{bmatrix} = A^{-1} \begin{bmatrix} \Sigma\delta_i \\ \Sigma\delta_i x_i \\ \Sigma\delta_i y_i \end{bmatrix} \tag{6}$$

where

$$A = \begin{bmatrix} N & \Sigma x_i & \Sigma y_i \\ \Sigma x_i & \Sigma x_i^2 & \Sigma x_i y_i \\ \Sigma y_i & \Sigma x_i y_i & \Sigma y_i^2 \end{bmatrix} \tag{7}$$

and all summations are over the reference stars. The uncertainties for the right ascension and declination are given by

$$\sigma_\alpha = \sqrt{\frac{\Sigma(\alpha_i - b_i - a_{11}x_i - a_{12}y_i)^2}{N-3}}, \sigma_\delta = \sqrt{\frac{\Sigma(\delta_i - b_2 - a_{21}x_i - a_{22}y_i)^2}{N-3}} \tag{8}$$

[12]. Both manual LSPR and automated LSPR from Astrometry.net were performed. In the end, the automated LSPR from Astrometry.net was used in the final calculation of the orbital elements of 2012 FN62.

Table 4: Results of LSPR on 2012 FN62

Date	α	δ
6/14	17:42:34.25	+13° 18' 30.84"
6/25	17:57:54.523	+12° 59' 26.44"
7/2	18:09:47.1284101698	+11°39' 49.509358176"
Date	σ_α	σ_δ
6/14	0.00010310917057221035	5.679631878320875e-05
6/25	3.9241819455363414e-05	5.694183098577491e-05
7/2	4.083777256619652e-05	2.6386330450746124e-05

4. Orbit Determination

4.1. Observation Selection

As previously discussed, the orbit of 2012 FN62 was calculated using the Method of Gauss. Although the asteroid was observed on six nights, three of the observations - those on June 12, 2024, June 23, 2024, and June 29, 2024 - were unusable due to factors such as light pollution, the faintness of the asteroid, and the proximity to a superior observation. As such, the observations on June 14, 2024, June 25, 2024, and July 2, 2024 were chosen to be used in the method.

4.2. Orbit Determination

Photometry and astrometry were applied to the best image of each observation to calculate the right ascension and the declination of 2012 FN62 at the times the images were taken. Alongside the times of observation, these coordinates were then inputted into a Python script that applied the Method of Gauss and calculated the six orbital elements. A test for consistency was performed afterward, wherein the right ascension and the declination for 2012 FN62 for the time of the third observation were predicted from the calculated orbital elements and compared to the actual (α_3, δ_3). The results from this test are discussed in section 5.2.

4.3. Monte Carlo Simulations

Applying the Method of Gauss and using the resulting position and velocity vectors for orbital determination is a long process that inevitably has some degree of error. The uncertainty of the results was estimated with a Monte Carlo simulation, wherein the inputted right ascension and declination values for each observation were slightly tweaked and the output orbital elements were recorded over 250,000 trials.

To randomize each trial of the simulation, the inputted values from each observation were selected using a Gaussian distribution whose mean and standard deviation are the mean and the standard deviation of the LSPR performed on the image. After all trials were complete, the distribution of the calculated values of each orbital element was plotted. The mean value of each distribution was taken to be the final result, and the final error was taken to be 3σ.

4.4. Results

Table 5: Orbital Elements of Asteroid 2012 FN62

Orbital Element	Calculated Value	Error (3σ)
a	3.3 AU	± 0.1 AU
e	0.615°	± 0.011
Ω	147.95°	± 0.02°
i	10.00°	± 0.11°
ω	142.47°	± 0.06°
M	356.60°	± 0.14°
T	2458361.2	± 0.1 JD

[4]

[4]The distributions of the Monte Carlo simulations for each orbital element are given in Appendix E.

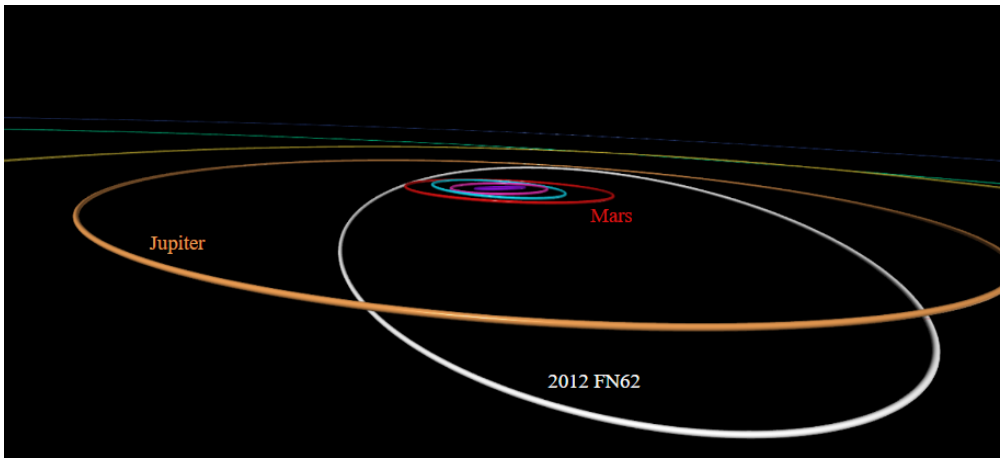


Figure 5: Orbit Visualization of 2012 FN62 [9]

5. Discussion of Results

5.1. Comparison to NASA's Jet Propulsion Laboratory Horizons System (JPL Horizons)

Table 6: Calculated Orbital Elements Compared with JPL Horizons

Orbital Element	Value (From Table 5)	JPL Horizons Value [10]	Difference
a	3.25585070215825 AU	3.262669109278968 AU	0.209201086073%
e	0.6152805534640687	0.6171254068924048	0.299390539754%
Ω	147.9524396466993°	147.9990226196437°	0.0314801437963%
i	9.996041075963197°	10.01081411395264°	0.147679761254%
ω	142.4702153304104°	142.4375221148329°	0.0229500369984%
M	356.6041444395877°	356.6201666258748°	0.00449288843314%
T	2458361.1658418924	2458353.4631981049	0.00313325317242%

The calculated values for the orbital elements in table 7 are all within 0.35% of the value on JPL Horizons. The discrepancy in the orbit would be explained if the asteroid was perturbed by a collision or by gravitational interactions. The latter would be more likely as the orbit of 2012 FN62 passes close to the orbits of Mars and Jupiter.

5.2. *Self-Consistency Check*

Table 7: Self-Consistency Check Results

Observation	Observed α	Generated α	Percent Error
6/14	17:42:34.250000	17:42:34.685863	0.000683661358763720 5%
7/2	18:09:47.1284101698	18:09:46.260960	0.001326638075650861 4%
Observation	Observed δ	Generated δ	Percent Error
6/14	+13:18:30.840000	+13:17:56.426359	0.07182850670238185%
7/2	+11:39:49.509358176	+11:39:9.730199	0.09473594755778052%

The results of the self-consistency check suggest that the Python script and orbital elements were accurate, since all errors were within 0.1%.

5.3. *Factors Affecting Observation Quality*

As Morehead Observatory is in close proximity to the town of Chapel Hill and the city of Durham, light pollution is extensive in the area, equivalent to that found in a bright suburban sky. As such, the Milky Way is not visible and the sky glows white within 35° above the horizon. Although the effects of light pollution can be mostly corrected through photometry, it still diminishes the contrast between the background sky and 2012 FN62, which was already very dim – the magnitude of the asteroid (∼17) (table 3) was only slightly less than the maximum magnitude of an object the telescope at Morehead can observe (∼18) [4]. Atmospheric humidity causes atmospheric seeing, decreasing the clarity of the asteroid. Additionally, with the close proximity of Morehead observatory to Durham and Chapel Hill, moderate levels of pollutants in the atmosphere would likely increase sky background noise and reduced the amount of light reaching the CCD, further impacting the contrast between the sky and 2012 FN62.

5.4. *Potential Improvements*

Most of the factors discussed in subsection 5.3 are not easily fixable. For example, although atmospheric seeing due to humidity as well as interference due to clouds and haze could be improved by observing at a superior time and location, with the limited time frame and single available telescope, better conditions for observation were not available.

However, a 4$^{\text{th}}$ observation would allow for differential corrections [14], a method that adjusts the orbit to account for an additional observation, and using the process of image stacking would keep the signal from the target object the same while averaging out random noise, increasing the quality of the images. The Python script that ran the Method of Gauss could also have been improved for precision.

6. Acknowledgements

We would like to thank Dr. Michael Hannawald, Dr. Suman Kumar, and Dr. Jose Manuel Zorrilla Matilla for their lectures, their eagerness to provide assistance throughout observations, problem sets, and programming, their inspiration of curiosity, and for always making sure that everybody understood and that no one was left behind.

Additionally, this research would never have been possible without the invaluable help of Dr. Jennifer Rosenthal, Sonya Dutton, Vishesh Goyal, Junu Lee, and Lucy Walton, who managed the program.

References

[1] IASC. Welcome to IASC.
[2] The Summer Science Program. Orbit Determination Package, 2024.
[3] MIT OCW. The solar system, 2006.
[4] Boller Chivens. 24-Inch (.61 meter) Telescope Specifications - Boller and Chivens.
[5] FLI. Proline PL09000.
[6] Diffraction Limited. Maxim DL.
[7] Keivan G. Stassun Frederic V. Hessman Karen A. Collins, John F. Kielkopf. AstroImageJ: Image Processing and Photometric Extraction for Ultra-Precise Astronomical Light Curves, 2016.
[8] Smithsonian Astrophysical Observatory. Saoimage ds9: A utility for displaying astronomical images in the X11 window environment, 2000.
[9] We would like to thank Luca Huang, Matek Gelt, and George Ji for their images from 6/25 that they allowed us to use as one of our three observations, as well as their orbit visualization code that they allowed us to use to create Figure 5.
[10] NASA. Horizons System, 2024.
[11] The Summer Science Program. Ccds and Image Calibration, 2024.
[12] The Summer Science Program. Astrometry, 2024.
[13] The Summer Science Program. Photometry, 2024.
[14] The Summer Science Program. AWR - MoG - Differential Correction, 2020.

Appendix A. The Method of Gauss

Appendix A.1. Initial Approximation

First, define the following:

$$k = 0.0172020989484 \tag{A.1}$$

$$\begin{cases} \tau_1 = k(t_1 - t_2) \\ \tau_3 = k(t_3 - t_2) \\ \tau_0 = k(t_3 - t_1) \end{cases} \tag{A.2}$$

$$\begin{cases} A_1 = \frac{\tau_3}{\tau_0} \\ B_1 = \frac{A_1}{6}(\tau_0^2 - \tau_3^2) \\ A_3 = \frac{-\tau_1}{\tau_0} \\ B_3 = \frac{A_3}{6}(\tau_0^2 - \tau_1^2) \end{cases} \tag{A.3}$$

$$\begin{cases} A = \frac{A_1 D_{21} - D_{22} + A_3 D_{23}}{-D_0} \\ B = \frac{B_1 D_{21} + B_3 D_{23}}{-D_0} \\ E = -2(\hat{\rho}_2 \cdot \vec{R}_2) \\ F = R_2^2 \end{cases} \tag{A.4}$$

$$\begin{cases} a = -(A^2 + AE + F) \\ b = -\mu(2AB + BE) \\ c = -\mu^2 B^2 \end{cases} \tag{A.5}$$

Then, define the 8^{th} degree polynomial

$$r_2^8 + a r_2^6 + b r_2^3 + c = 0 \tag{A.6}$$

where the positive, real roots of the polynomial are possible values for r_2. Afterwards, define

$$u = \frac{1}{r_2^3} \tag{A.7}$$

$$\begin{cases} f_i = 1 - \frac{1}{2} u \tau_i^2 \\ g_i = \tau_i - \frac{1}{6} u \tau_i^3 \end{cases} \quad \text{for } i \in \{1, 2, 3\} \tag{A.8}$$

$$\begin{cases} c_1 = \frac{g_3}{f_1 g_3 - g_1 f_3} \\ c_2 = -1 \\ c_3 = \frac{-g_1}{g_1 g_3 - g_1 f_3} \\ d_1 = \frac{-f_3}{f_1 g_3 - f_3 g_1} \\ d_3 = \frac{f_1}{f_1 g_3 - f_3 g_1} \end{cases} \tag{A.9}$$

$$\begin{cases} D_0 = \hat{\rho_1} \cdot (\hat{\rho_2} \times \hat{\rho_3}) \\ D_{1i} = (\vec{R_i} \times \hat{\rho_2}) \cdot \hat{\rho_3} \\ D_{2i} = (\hat{\rho_1} \times \vec{R_i}) \cdot \hat{\rho_3} \\ D_{3i} = \hat{\rho_1} \cdot (\rho_2 \times \vec{R_i}) \end{cases} \quad \text{for } i \in \{1, 2, 3\} \tag{A.10}$$

$$\begin{cases} \rho_1 = \frac{c_1 D_{11} + c_2 D_{12} + c_3 D_{13}}{c_1 D_0} \\ \rho_2 = \frac{c_1 D_{21} + c_2 D_{22} + c_3 D23}{c_2 D_0} \\ \rho_3 = \frac{c_1 D_{31} + c_2 D32 + c_3 D_{33}}{c_3 D_0} \end{cases} \tag{A.11}$$

Finally, calculate estimates of $\vec{r_1}$, $\vec{r_2}$, and $\vec{r_3}$ through equation 1 and approximate $\dot{\vec{r_2}}$ by

$$\dot{\vec{r_2}} = d_1 \vec{r_1} + d_3 \vec{r_3} \tag{A.12}$$

Appendix A.2. Iteration and Convergence

Next, improve the approximation of $\vec{r_2}$ and $\dot{\vec{r_2}}$ through the following process:

$$\begin{cases} u = \frac{1}{r_2^3} \\ z = \frac{\vec{r_2} \cdot \dot{\vec{r_2}}}{r_2^2} \\ q = \frac{\dot{\vec{r_2}} \cdot \dot{\vec{r_2}}}{r_2^2} - u \end{cases} \tag{A.13}$$

$$\begin{cases} \tau_1 = k(t_1 - t_2) \\ \tau_3 = k(t_3 - t_2) \\ \tau_0 = k(t_3 - t_1) \end{cases} \tag{A.14}$$

$$\begin{cases} f_i = 1 - \frac{1}{2} u \tau_i^2 + \frac{1}{2} u z \tau_i^3 + \frac{1}{24}(3uq - 15uz^2 + u^2)\tau_i^4 \\ g_i = \tau_i - \frac{1}{6} u \tau_i^3 + \frac{1}{4} u z \tau_i^4 \end{cases} \quad \text{for } i \in \{1, 2, 3\} \tag{A.15}$$

$$\begin{cases} c_1 = \frac{g_3}{f_1 g_3 - g_1 f_3} \\ c_2 = -1 \\ c_3 = \frac{-g_1}{g_1 g_3 - g_1 f_3} \\ d_1 = \frac{-f_3}{f_1 g_3 - f_3 g_1} \\ d_3 = \frac{f_1}{f_1 g_3 - f_3 g_1} \end{cases} \tag{A.16}$$

$$\begin{cases} \rho_1 = \frac{c_1 D_{11} + c_2 D_{12} + c_3 D_{13}}{c_1 D_0} \\ \rho_2 = \frac{c_1 D_{21} + c_2 D_{22} + c_3 D23}{c_2 D_0} \\ \rho_3 = \frac{c_1 D_{31} + c_2 D32 + c_3 D_{33}}{c_3 D_0} \end{cases} \tag{A.17}$$

Correct for light travel time by redefining t_i as $t_i' - \frac{\rho_i}{c}$ for $i \in \{1, 2, 3\}$, where t_i' is the original observation time, in Julian days, of the ith observation. Finally, calculate $\vec{r_1}$, $\vec{r_2}$, and $\vec{r_3}$ through equation 1 and approximate $\dot{\vec{r_2}}$ by

$$\dot{\vec{r_2}} = d_1 \vec{r_1} + d_3 \vec{r_3} \tag{A.18}$$

Repeat the process until ρ_2 converges. Afterwards, the values of $\vec{r_2}$ and $\dot{\vec{r_2}}$ will be the final vectors produced by the Method of Gauss.

Appendix B. Calculation of the Orbital Elements

$$\vec{h} \equiv \text{Angular Momentum} = \vec{r} \times \dot{\vec{r}} \tag{B.1}$$

$$a \equiv \text{Semi-Major Axis Length} = \frac{1}{\frac{2}{r} - \dot{\vec{r}} \cdot \dot{\vec{r}}} \tag{B.2}$$

$$e \equiv \text{Eccentricity} = \sqrt{1 - \frac{h^2}{a}} \tag{B.3}$$

$$i \equiv \text{Inclination} = \arctan\left(\frac{\sqrt{h_x^2 + h_y^2}}{h_z}\right) \tag{B.4}$$

$$\Omega \equiv \text{Longitude of the Ascending Node} = \arctan\frac{h_x}{-h_y} \tag{B.5}$$

$$\nu \equiv \arctan\left(\frac{(\vec{r} \cdot \dot{\vec{r}})(1 - e^2)}{h(a(1 - e^2) - r)}\right) \tag{B.6}$$

$$\omega \equiv \text{Argument of Perihelion} = \arctan\left(\frac{r_z}{(r_x cos(\Omega) + r_y sin(\Omega))sin(i)}\right) - \nu \tag{B.7}$$

$$E \equiv \arctan\frac{rsin(\nu)(1 + ecos(\nu)}{a(1 - e^2)(e + cos(\nu)} \tag{B.8}$$

$$M \equiv \text{Mean Anomaly} = E - esin(E) \tag{B.9}$$

$$k \equiv 0.0172020989484 \tag{B.10}$$

$$T \equiv \text{Time of Last Perihelion Passage} = \text{Current Julian Date} - M\sqrt{\frac{a^3}{k}} \tag{B.11}$$

Appendix C. Derivation of LSPR

After recording the (x, y) locations of many known reference stars on the image alongside their actual α values and the ones predicted by the linear transformation, the χ^2 test statistic for the right ascension transformation can be calculated:

$$\chi^2_\alpha = \Sigma(observed - expected)^2 = \Sigma(\alpha - b_1 - a_{11}x - a_{12}y)^2 \tag{C.1}$$

To minimize χ^2_α, differentiate (A.1) with respect to a_{11}, a_{12}, and b_1:

$$\begin{cases} \frac{\partial^2 \chi^2_\alpha}{\partial b_1^2} = 0 \implies \sum\Big(-2(\alpha_i - b_1 - a_{11}x_i - a_{12}y_i)\Big) & = 0 \\ \frac{\partial^2 \chi^2_\alpha}{\partial a_{11}^2} = 0 \implies \sum\Big(-2x_i(\alpha_i - b_1 - a_{11}x_i - a_{12}y_i)\Big) & = 0 \\ \frac{\partial^2 \chi^2_\alpha}{\partial a_{12}^2} = 0 \implies \sum\Big(-2y_i(\alpha_i - b_1 - a_{11}x_i - a_{12}y_i)\Big) & = 0 \end{cases} \tag{C.2}$$

$$\begin{cases} \Sigma(\alpha_i - b_1 - a_{11}x_i - a_{12}y_i) & = 0 \\ \Sigma(x_i(\alpha_i - b_1 - a_{11}x_i - a_{12}y_i)) & = 0 \\ \Sigma(y_i(\alpha_i - b_1 - a_{11}x_i - a_{12}y_i)) & = 0 \end{cases} \tag{C.3}$$

$$\begin{cases} \Sigma\alpha_i - b_1 N - a_{11}\Sigma x_i - a_{12}\Sigma y_i = 0 \\ \Sigma x_i\alpha_i - b_1\Sigma x_i - a_{11}\Sigma x_i^2 - a_{12}\Sigma x_i y_i = 0 \\ \Sigma y_i\alpha_i - b_1\Sigma y_i - a_{11}\Sigma x_i y_i - a_{12}\Sigma y_i^2 = 0 \end{cases} \tag{C.4}$$

$$\begin{bmatrix} \Sigma\alpha_i \\ \Sigma\alpha_i x_i \\ \Sigma\alpha_i y_i \end{bmatrix} = \begin{bmatrix} b_1 \\ a_{11} \\ a_{12} \end{bmatrix} \begin{bmatrix} N & \Sigma x_i & \Sigma y_i \\ \Sigma x_i & \Sigma x_i^2 & \Sigma x_i y_i \\ \Sigma y_i & \Sigma x_i y_i & \Sigma y_i^2 \end{bmatrix} \tag{C.5}$$

$$\begin{bmatrix} b_1 \\ a_{11} \\ a_{12} \end{bmatrix} = A^{-1} \begin{bmatrix} \Sigma\alpha_i \\ \Sigma\alpha_i x_i \\ \Sigma\alpha_i y_i \end{bmatrix} \tag{C.6}$$

where

$$A = \begin{bmatrix} N & \Sigma x_i & \Sigma y_i \\ \Sigma x_i & \Sigma x_i^2 & \Sigma x_i y_i \\ \Sigma y_i & \Sigma x_i y_i & \Sigma y_i^2 \end{bmatrix} \tag{C.7}$$

, N is the total number of reference stars, and the summations are for every reference star used in a particular observation. Using a similar process for declination yields

$$\begin{bmatrix} b_2 \\ a_{21} \\ a_{22} \end{bmatrix} = A^{-1} \begin{bmatrix} \Sigma\delta_i \\ \Sigma\delta_i x_i \\ \Sigma\delta_i y_i \end{bmatrix} \tag{C.8}$$

Appendix D. Calibration Images

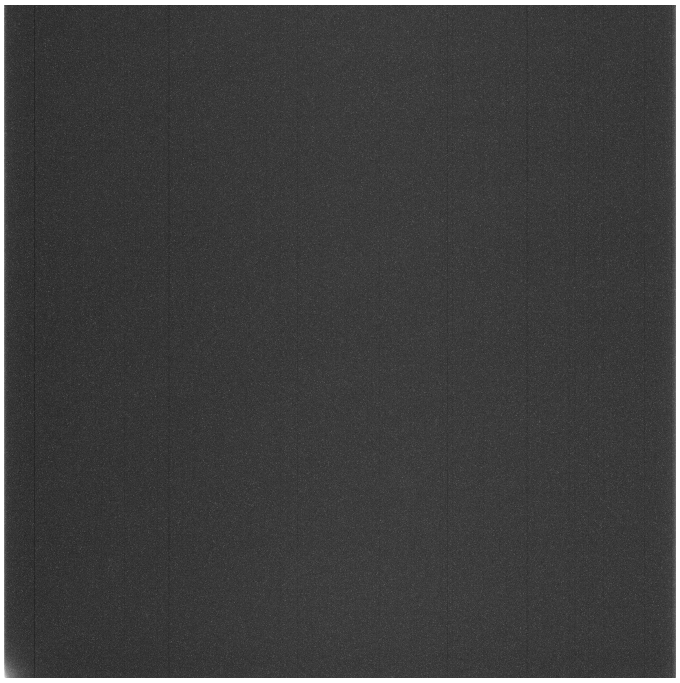


Figure D.6: Master Dark (With Bias) Used in Image Reduction

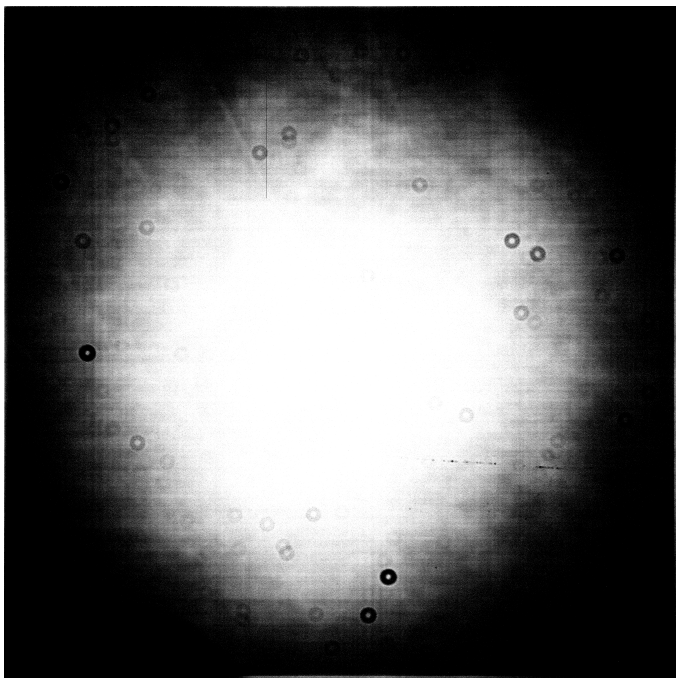
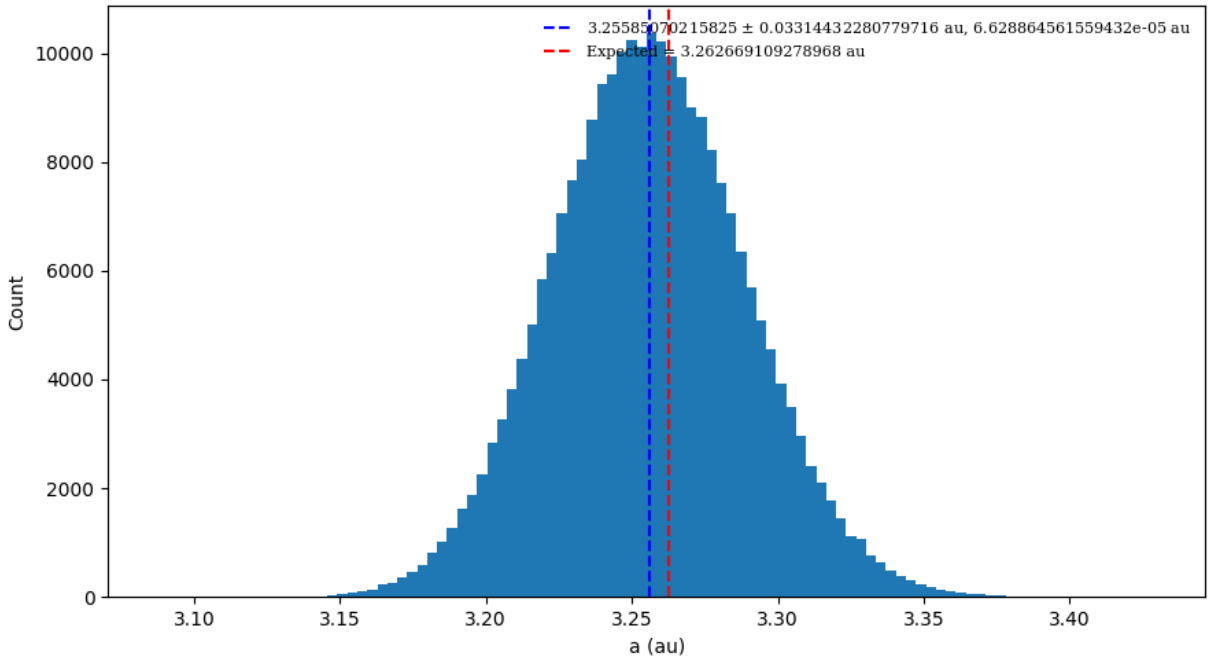
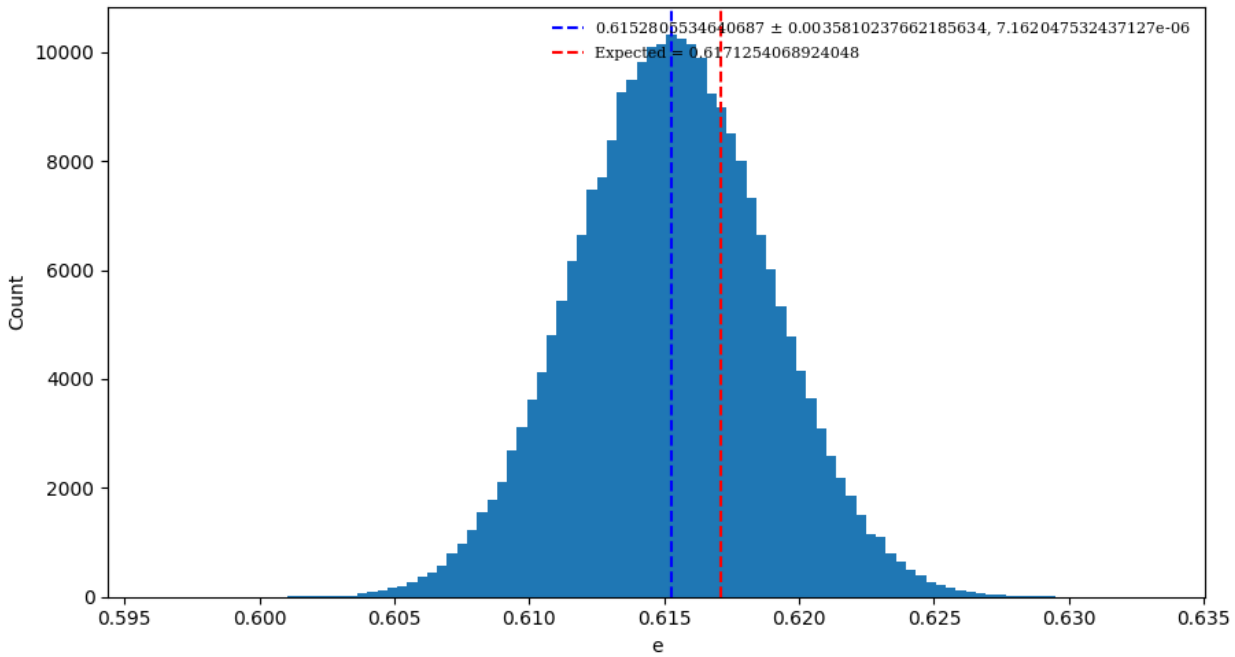
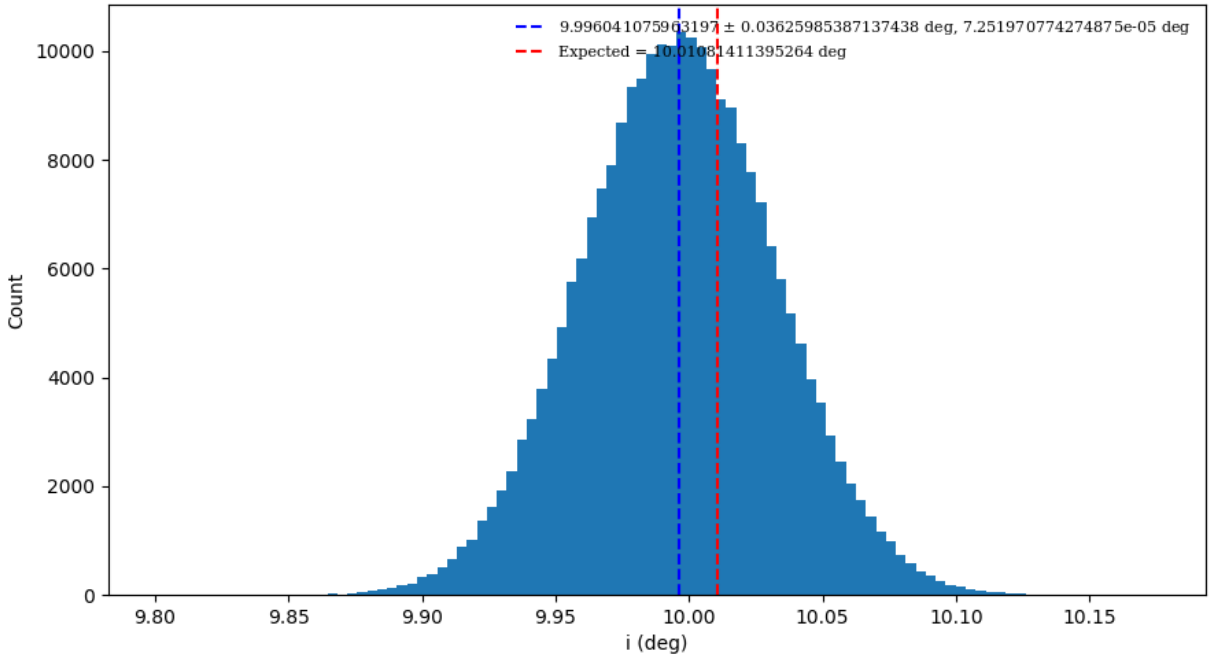


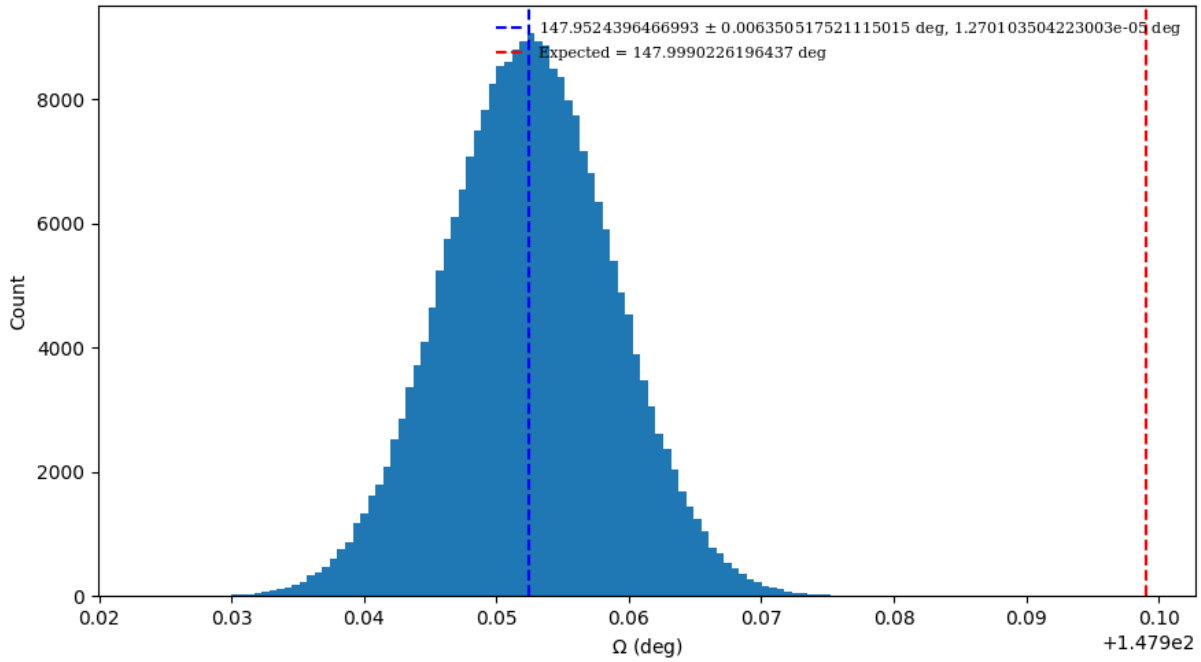
Figure D.7: Normalized Master Flat Used in Image Reduction

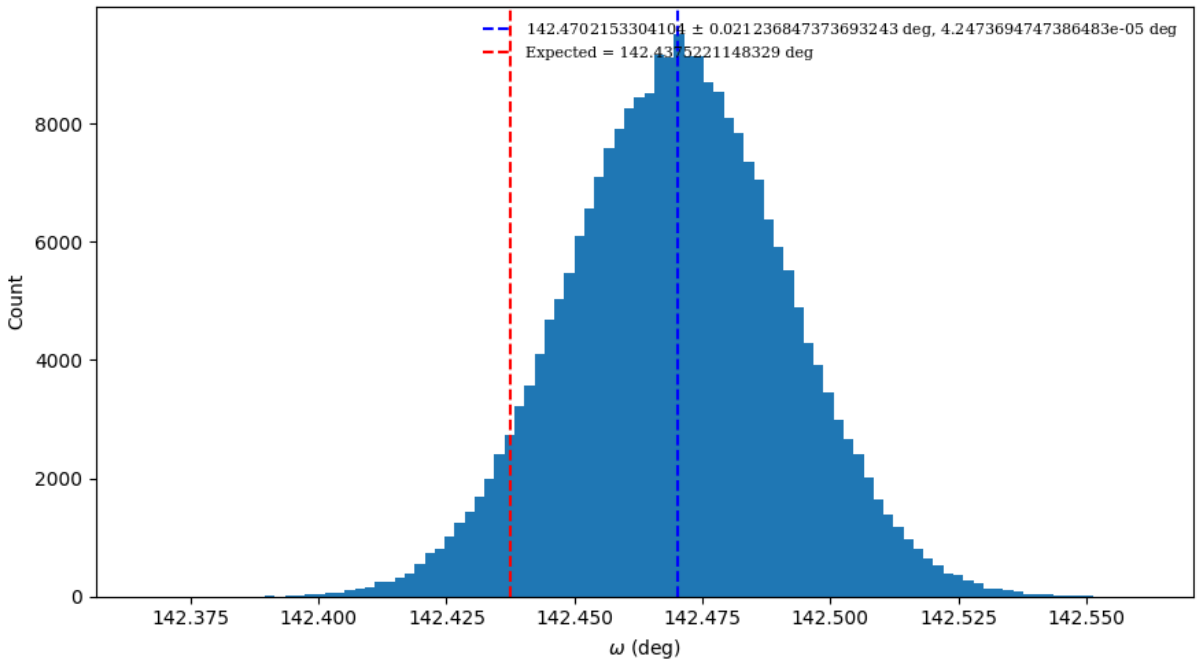
Appendix E. Results of Monte Carlo Simulations

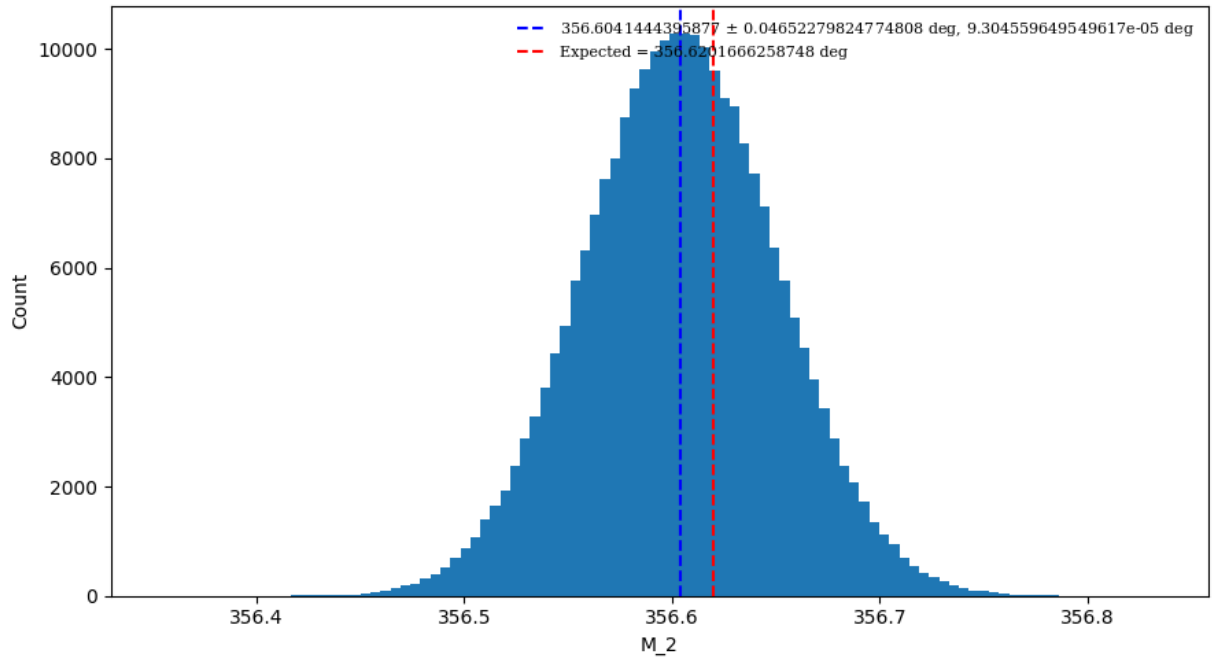





9.996041075963197 ± 0.03625985387137438 deg, 7.251970774274875e-05 deg
Expected = 10.01081411395264 deg
Count
i (deg)


147.9524396466993 ± 0.006350517521115015 deg, 1.270103504223003e-05 deg
Expected = 147.9990226196437 deg
Count
Ω (deg)
+1.479e2


142.4702153304104 ± 0.021236847373693243 deg, 4.2473694747386483e-05 deg
Expected = 142.4375221148329 deg
Count
8000
6000
4000
2000
0
142.375
142.400
142.425
142.450
142.475
142.500
142.525
142.550
ω (deg)


356.6041444395877 ± 0.04652279824774808 deg, 9.304559649549617e-05 deg
Expected = 356.6201666258748 deg
Count
10000
8000
6000
4000
2000
0
356.4
356.5
356.6
356.7
356.8
M_2